NTNU – Trondheim
Norwegian University of
Science and Technology

FFI Forsvarets forskningsinstitutt
Norwegian Defence Research Establishment

Monte Carlo Simulation of Photoconductive Terahertz Sources in Mercury Cadmium Telluride

Théophile Chirac

June 2016

MASTER THESIS

Norwegian University of Science and Technology

Norwegian Defence Research Establishment

Supervisor 1: Jon Støvneng (NTNU)

Supervisor 2: Trond Brudevoll (FFI)

Supervisor 2: Asta Storebø (FFI)

Preface

This Master's thesis in physics was written during the academic year autumn 2015 - spring 2016 for the Natural Science faculty of the Norges Teknisk-Naturvitenskapelige Universitet (NTNU). It was done in cooperation with the Forsvarets Forskningsinstitutt (FFI), which provided documentation and all the required softwares. The present work closes a Double Degree in physics and engineering, in agreement with NTNU and the École Centrale de Lyon.

The content of this thesis treats topics related to semiconductor physics, and is presumed to be read by a common university level physics student. The reader is assumed to have fundamental knowledge about solid state physics.

Trondheim, 2016-05-15

Théophile Chirac

Acknowledgment

I would like to thank Trond Brudevoll and Asta-Katrine Storebo for their very warm welcome at FFI and for the proposal of the master's thesis. I am also particularly grateful for Trond's fast and helpful feedbacks that helped me a lot to have a grip on the project.

I would like to address all my gratitude to Jon Andrea Støvneng who has made the collaboration with FFI possible and who was always receptive to help me with NTNU's infrastructures and administrative procedures when required.

Finally, many thanks are aimed at Peder Brenne, who helped me integrate the master of physics, even though tweaking the usual procedures was necessary within the context of a double degree.

T.C.

To all my friends in the endlessly charming city of Trondheim.

Abstract

In this master's thesis we explore the physics of a photoconductive terahertz emitter and diverse methods to increase its power emission. A way to simulate it via a Monte Carlo first principle simulator is presented, taking into account propagation delays. We show that the simulator is successfully in representing an increase of power with a lowering of the effective mass, an increase of the bias voltage or a stronger laser beam, and that the optical excitation should be focused on the vicinity of the anode. Discussions on screening and scattering effects, along with possible ways to improve the model are addressed.

Contents

Chapter 1

Introduction

1.1 Background

A wide range of technology use the physics of radiation, and it has been shown over the years that mastering a certain wavelength can lead to major technological breakthroughs. A clear illustration of this is infra-red DVDs being replaced by Blue Rays, the later offering a much denser information support, mainly because the blue-violet wavelength used is significantly smaller. Imaging reveals also a much broader range of information when one look beyond the narrow visible spectrum. Mastering the whole electromagnetic spectrum is therefore of huge interest, yet, a well-known technological gray area known as the *terahertz gap* screens our possibilities. Indeed, due to the relatively recent emergence of interest in this range, technologies to produce, detect and reflect radiations at these frequencies are quite rare, or of limited power, even if it would provide several technological improvements, ranking form medical imaging, airport security checks, astronomy exploration and non intrusive quality-control,... among others [4, 9, 14, 2].

1.2 Objectives

FFI is investigating this promising area. The team I joined works on semiconductor devices, and would like to simulate a terahertz (THz) emitter based on semiconductor technology. It has

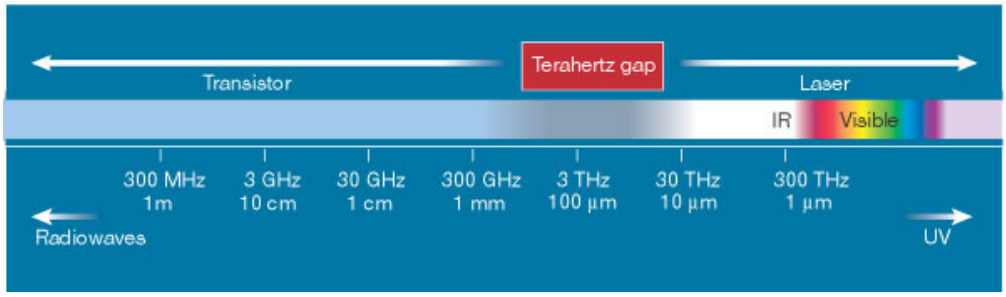

Figure 1.1: The THz gap is due to a disconnection between electronics and optics technologies.[13]

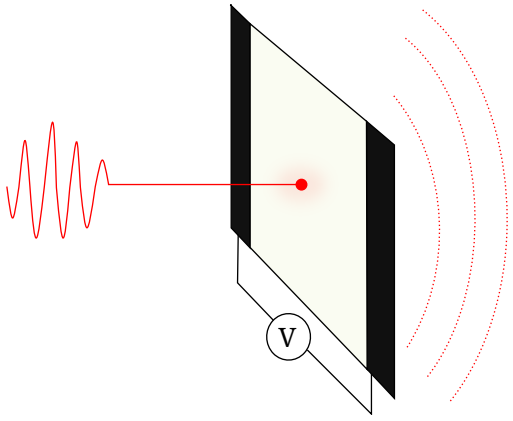

Figure 1.2: Photoconductive switch: a femtosecond laser pulse excites a biased semiconductor, emitting THz radiations.

been shown that a semiconductor excited by a proper laser impulsion emits THz radiation and that this technique offers several axis of optimization [7]. A goal of this master's thesis is to implement this effect in a first-principle Monte Carlo simulator, and provide proper visualizations that can show major tendencies and lead to an improvement of such a THz emitter.

1.3 Limitations

We simulate a so-called photoconductive switch: the device consists of a piece of semiconductor —in our case $Cd_xHg_{1-x}Te$, with $x = 0.28$ — between two electrodes; a voltage is applied between the electrodes, and an laser excitation is focused in between (Figure 1.2). The laser excitation creates free charges in the semiconductor that are accelerated by the tension, generating THz radiation. Such a device has typically dimensions in the orders of tens of micrometers. The current technology is limited by effects occurring fractions of a second after excitation and

limiting efficiency, mainly scatterings and self-screening of the electric field by the carriers, leading to a saturation of the output radiation. A fine study on these screening effects that we develop in this thesis could lead to technological improvements.

1.4 Approach

Our research group already have a 2D analytic first principle semiconductor simulator they work on. It is a Poisson solver and a Monte Carlo simulator dealing with carrier scattering, written in Fortran 90. The work of this master's thesis uses it as a basis.
A first point of interest is the implementation of a photoconductive source and the associated physical phenomena in this simulator, secondly the analysis of the simulation. The possible sensitive parameters for optimizing the THz emission considered in this thesis are

- the composition of the medium,
- the strength of the bias field,
- the power of the laser excitation,
- the position of the laser spot,
- the shape of the laser spot and
- the duration of the laser excitation.

1.5 Structure of the thesis

Following this introduction, Chapter 2 gives the frame of the model we are using and describes the basics of the first principle simulator, Chapter 3 concentrates on the implementation in the simulator of the terahertz radiation, along with other features that could lead to an increase of yield. Chapter 4 presents our results and physical discussions of the phenomenon at hand for our parameters. The last chapter sums up our work.

Chapter 2

Approach: Monte Carlo First Principle Simulator

The program on which our studies are carried out is a first principle simulator, meaning it tries to simulate physics according to all the relevant known physics laws at lowest level (i.e. electronic level). It relies on Monte Carlo method, meaning that a large number of test carriers are simulated to get a significant statistical result. The program simulates carriers transport, several scattering mechanisms and integrates a Poisson solver. All the numerical computations in this work revolve around a mesh of our device: it consists in a subdivision of the domain into a finite number of cells for which we can compute physics locally, and in which particles such as electrons and holes are evolving accordingly.

2.1 Superparticles

Due to the limited resources of the available computers, it is inconceivable to simulate as many electrons as there is in an actual sample. The simulation relies on *superparticles*, which behave and have the dynamics of single particles, but influence the surrounding space as if their charge were those of many. Thanks to superparticles, physically correct order of magnitude can be computed (electric fields, free carrier densities, etc.). For a given number of real particles, the more superparticle the simulation handles, the more physically accurate it gets. To keep reasonable computing times for our simulations, we simulate only a few 10 000 superparticles. Indeed,

the radiation computation time increases as the number of superparticles times the number of vertices in the mesh of the device, and such computation must be done at each time step. Only with more time at disposal or faster computers could we afford to improve precision.

2.2 Semi-classical model

The model we use is semi-classical, in a sense that motion of the carriers is dictated from classical mechanics, with both determined position and momentum, yet we also take into account quantum effects from the band model and scattering mechanisms.

In the following, $\mathbf{p}$ denotes the momentum of a carrier (electron or hole), and $\mathbf{k}$ its wave vector. The time variable and a time interval are respectively denoted t and Δt. $\mathbf{E}$ stands for the electric field. Subscripts refer to the time the variable is evaluated at.

To numerically compute the dynamics of a carrier, we use Newton's laws of motion in a discrete approximation and the $\mathbf{k}$–$\mathbf{p}$ relation to get a discrete relation for $\mathbf{k}$:

$$\mathbf{p}_{t+\Delta t} \simeq \mathbf{p}_t + q\mathbf{E}\Delta t \tag{2.1a}$$

$$\mathbf{p} = \hbar\mathbf{k} \tag{2.1b}$$

$$\mathbf{k}_{t+\Delta t} \simeq \mathbf{k}_t + \frac{q\mathbf{E}}{\hbar}\Delta t \tag{2.1c}$$

The positions $\mathbf{x}$ of the carriers are obtained thanks to the leap-frog method:

$$\mathbf{x}_{t+\Delta t} \simeq \mathbf{x}_t + \frac{\mathbf{v}_{t+\Delta t} + \mathbf{v}_t}{2}\Delta t \tag{2.2}$$

To take the nonparabolicity of the bands of the material into account, the velocity is computed as follows [7, p15]:

$$\mathbf{v} = \frac{\hbar\mathbf{k}}{m^\star\,(1 + 2\alpha\mathscr{E})} \tag{2.3}$$

where α is a non parabolic factor and $\mathscr{E}$ the energy of the particle. If we note m_{eff} the electron effective mass, $m^\star$ the electron effective mass at the bottom of the band, m_0 the free electron

mass, and $\mathscr{E}_g$ the bandgap energy, we have:

$$\mathscr{E} = \frac{-1+\sqrt{1+4\alpha\gamma}}{2\alpha} \tag{2.4a}$$

$$\alpha = \frac{1}{\mathscr{E}_g}\left(1-\frac{m^\star}{m_0}\right)^2 \tag{2.4b}$$

$$\gamma = \frac{\hbar^2\mathbf{k}^2}{2m_{\text{eff}}} \tag{2.4c}$$

2.3 Scattering mechanisms

The program simulates the many possible scatterings of a carriers (electron or hole) between its free flights. The types of scattering are selected randomly according to their real likelihood. Thus, the program deals with

- polar optical phonon scattering (absorption/emission),
- non-polar optical phonon scattering (absorption/emission)
- acoustic phonon deformation potential (absorption/emission),
- ionized impurity scattering,
- inter-valley scattering (absorption/emission),
- electron-plasmon (absorption/emission),
- alloy scattering[1],
- electron-electron scattering[1],
- electron-hole scattering[1],
- hole-hole scattering[1],
- impact ionization scattering

Their implementation is described in Ref [7].

2.4 Poisson solver

To compute the **E** field in Equation 2.1a, a common method is to use a Poisson solver, which by definition aims at solving the Poisson equation:

$$\nabla^2\phi = -\frac{\rho}{\epsilon} \tag{2.5}$$

[1] Not fully supported in the current simulator

Equation (2.5) is deduced from Maxwell's equations using the Coulomb gauge $\nabla.\mathbf{A} = 0$ for the vector potential. Such an equation can be solved numerically with an iterative finite-difference method. The electric field is then deduced from the definition of the potentials:

$$\mathbf{E} = -\nabla\phi - \frac{\partial \mathbf{A}}{\partial t} \tag{2.6}$$

In a static context, or a semi-static context (where radiation is not of interest), the second term of equation (2.6) can be dropped, and getting $\mathbf{E}$ from ϕ with the finite-difference method is straightforward. Unfortunately, in a more general context, $\mathbf{A}$ must be computed. This in not always an easy task since $\mathbf{A}$ and ϕ are coupled in the Coulomb gauge; in homogeneous media this is through the equation:

$$\nabla^2\mathbf{A} = \mu\epsilon\frac{\partial^2\mathbf{A}}{\partial t^2} + \mu\epsilon\nabla\frac{\partial\phi}{\partial t} - \mu\mathbf{j} \tag{2.7}$$

The coupling is due to the fact that in the Coulomb gauge, ϕ is instantaneous, even though $\mathbf{A}$, $\mathbf{E}$ and $\mathbf{B}$ are retarded. If one would like to re-establish symmetry, and uncouple $\mathbf{A}$ and ϕ, Lorentz gauge should be considered instead (Appendix A).

As a consequence, a Poisson solver is of interest when it comes to deal with static charges, such as impurity atoms, but is limited when it comes to accelerated charges. Due to limitations of Poisson equation in a radiative context, we present in section 3.1 a different method to obtain the $\mathbf{E}$ field from accelerated charges.

To solve equation 2.5 on our device, boundary conditions should be provided. In our case we impose the value of the potential ϕ on contacts (Dirichlet boundary condition), and Neumann boundary conditions on the other edges. The right hand side of the Poisson equation is determined by the amount of impurities and static charges. The numerical solution will deliver a static electric field, to which one should add the contribution from moving charges.

2.5 Device

In our simulator, particles bounce on edges and can be absorbed by contacts. The semiconductor we use is $Cd_xHg_{1-x}Te$, with $x = 0.28$ at working temperature 77 Kelvin. Material-related parameters such as the electric permittivity ε are supplied accordingly. Other parameters such

as device dimensions, size of the electrodes, impurity density and positions of the laser can be easily changed. When not specified otherwise, dimensions are $40\,\mu m \times 40\,\mu m$, and the laser spot is centred. Impurities densities are taken to be $10^{14}\,cm^{-3}$. The bias field is applied through Dirichlet conditions on the side contacts; fields of at least $4\,kV\,cm^{-1}$ are required [12], we typically work with $40\,kV\,cm^{-1}$ by applying a 160 V potential difference over the $40\,\mu m$-long device.

Chapter 3

TeraHertz emission

3.1 Radiation

3.1.1 Theory

A point charge q moving at velocity $\mathbf{v}$ and acceleration $\mathbf{a}$ generates an electric field at distance R in unitary direction $\widehat{\mathbf{R}}$ given by [7, 6]:

$$\mathbf{E} = \frac{q}{4\pi\varepsilon}\left(\frac{1}{\left|1-\widehat{\mathbf{R}}\cdot\mathbf{v}/c\right|}\left(\frac{\left(1-v^2/c^2\right)\left(\widehat{\mathbf{R}}-\mathbf{v}/c\right)}{R^2}+\frac{\widehat{\mathbf{R}}\times\left(\left(\widehat{\mathbf{R}}-\mathbf{v}/c\right)\times\mathbf{a}\right)}{c^2R}\right)\right)_{t_r} \tag{3.1}$$

Where the index t_r means "retarded time", and relates to the values inside the parenthesis taken at time $t_r = t - R/c$, with t being the present time. c is the speed of light. Electron and holes, moving at a speed significantly below the speed of light in our device (Fermi velocity is $1\times10^6\,\mathrm{m\,s^{-1}}$ [1], while light velocity in $Cd_xHg_{1-x}Te$ is $8.6\times10^7\,\mathrm{m\,s^{-1}}$) the previous expression can consequently be simplified as follow [7] :

$$\mathbf{E} \simeq \frac{q}{4\pi\varepsilon}\left(\frac{\widehat{\mathbf{R}}}{R^2}\right)_{t_r} + \frac{q}{4\pi\varepsilon c^2}\left(\frac{\widehat{\mathbf{R}}\times\left(\widehat{\mathbf{R}}\times\mathbf{a}\right)}{R}\right)_{t_r} \tag{3.2}$$

The two terms can be seen as the Coulomb field and the radiated field:

$$\mathbf{E} = \mathbf{E}_c + \mathbf{E}_r \tag{3.3}$$

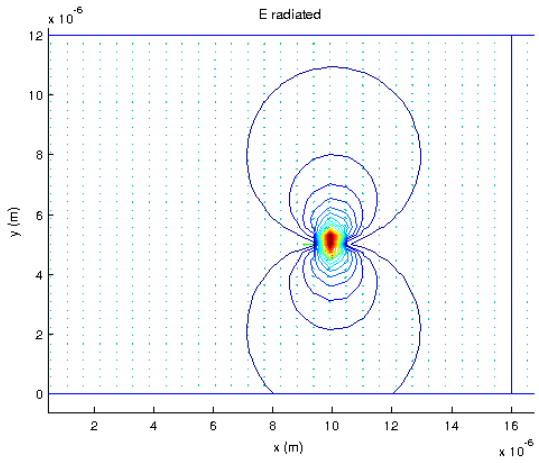

Figure 3.1: Strength of the radiated electric field from an electron-hole pair. Electron is accelerated to the left, hole to the right, radiation fields add up and create a distinctive toriodal radiation pattern.

The Coulomb field is a static field fading as R^{-2}, wereas the radiated field is proportional to the acceleration of the carrier and fades as R^{-1}. The radiated field has therefore a larger range, and is truly the one expected to produce THz emissions. Its shape from a single hole-electron pair is represented on Figure 3.1.

To compute the electric field in an outside the device, equation (3.2) was used for each carrier rather than from ϕ given by the Poisson solver. Indeed, we focus on a transient regime, at femtosecond timescales, for which light propagation delay cannot be neglected. Our device dimensions being 40 µm × 40 µm, and the speed of light in our medium roughly 8.6×10^7 m s^{-1} (for $Cd_xHg_{1-x}Te$, $\varepsilon_\infty = 3.5^2$), it takes about 0.5 ps for the electric field to cross the device, and approximately the same time to travel 150 µm outside the device. The delayed propagation is illustrated Figure 3.2.

This retarded radiation computation needs some attention to co-exist within the context of a Poisson solver designed for non-retarded fields (see discussion in Appendix A).

Inside the device, the static field from the electrodes obtained through the Poisson solver is added to the radiation field, since it is crucial for carrier motion. Outside the device, we need to neglect the electrode field, which is not a real issue since outside the device we are only interested in the radiated field. There, the electrode field, being static, does not interfere with the terahertz radiation.

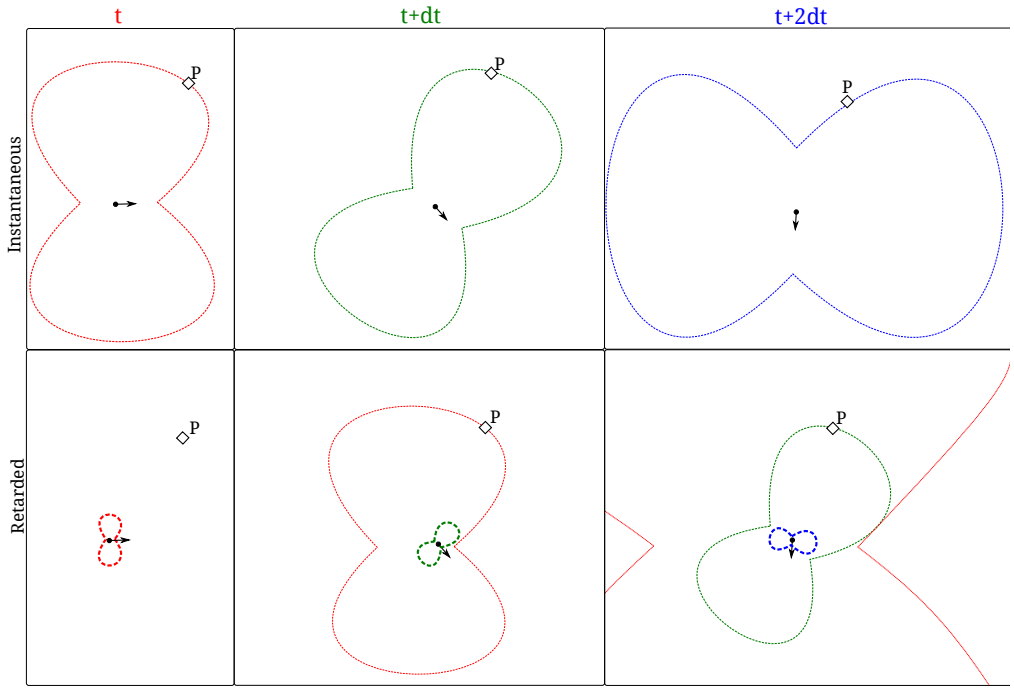

Figure 3.2: Computing the retarded signal at point P requires to know the position and acceleration of the particle at earlier times.

3.1.2 Algorithm

Delay: To take the delay of propagation into account, we rely on the fact that mesh points are not moving, only waiting for the field to reach them. We can therefore compute the field at time t from each carrier for each mesh point, and set a delay before the field actually apply. We store all the values of the forthcoming field in an array, in which all contributions from different carriers and different times can be added.

$$E_{\text{forthcoming}}(t) = [E(t), E(t+dt), ..., E(t+\max dt)] \tag{3.4}$$

In this table, only the first value (present time t) is definitive: in the next timestep, the carrier contributions at $t+dt$ is added to $[E(t+dt), ..., E(t+(\max+1)dt)]$, and all indices then shift one index to the left. max dt is given by the longest distance possible in the simulation between carriers and measure points, divided by the light speed in the medium. The number of elements in the array depend on the time between two updates.

Measure points: The Electric field is evaluated at 2 different kinds of points: on the mesh nodes, and at specific points outside the device editable by the user. On the later kind, all the values of E recorded over the simulation are stored in a single array:

$$E_{\text{measure}} = [E(0), ..., E(t), ..., E(t_{\text{final}})] \tag{3.5}$$

To fill this array, we used a method similar to the one previously described: at time t, the electric field from each carrier is computed and added to the cell of index $t + R_i/c$, where R_i is the distance to carrier i at time t. As previously, this method assumes the measuring point in not moving. The values between t_{final} (final simulation step time) and $t_{\text{final}} + R_{\text{max}}/c$ (the time at which the measure point will receive the t_{final}-contribution from the most remote carrier) shall be ignored, because not all contributions will have been computed.

3.2 Screening mechanism

The major effects and limitations one faces when dealing with photoconductive terahertz emitter are due to screening of the carriers. Fractions of a second after the laser excitation, photoexcited carriers will move towards the electrode, leading to a polarization of the device. This polarization screens out the bias field which therefore does not accelerate the particles as much as it would at earlier times. We can distinguish *Coulomb screening* and *radiative screening*, depending on whether the screening is static or due to acceleration of the charges.

Handling screening in our program was not as easy at it might appear. Main difficulty was to avoid particles getting too close to one another due to the divergence of the electric field as R tends to zero. Such divergences are merciless in a discrete time step context; if no care is taken, particles could be accelerated to the other side of the device in a single time step (ignoring scattering and incidentally cause a parasite radiation). This problem does not usually occur with the Poisson solver method since the particle in cell approach smooths the charge singularities within a charge density matrix.

We took this mechanism as an inspiration and gathered all the charges at the center of their cells to compute the Electric field at all the corners. It ensures R to be at least greater than half

a cell edge. In the dynamic phase, particles are assumed to feel the field from the closest vertex from them, *minus* the field they emitted themselves [1].

Particle-in-cell simulations are reputed to be stable when particles move at most of one cell per time step [10]. We fulfilled this condition taking 0.8 µm as cell size and a time step of 10 fs (electrons don't go faster than 10×10^5 m s^{-1}).

3.3 Laser pulse

3.3.1 Power intensity

The most natural way to enhance the power of the terahertz output is to increase the excitation input. In other words, if one increases the power of the laser, one can expect to reach a higher accelerated carrier density in the device and therefore a stronger radiation. When not specified, both carrier (electrons and holes) densities are assumed to be on average 10^{17} cm^{-2} on the laser spot. The excitons generated from the photons are given wave vectors following a Maxwellian distribution and respecting Pauli filling. They must also enforce energy and momentum conservation of the initial photon $\gamma \rightarrow e^- + h^+$.

3.3.2 Laser spatial parameters

Location

The spatial location of the optical excitation is known to play a significant role in the THz emission. In GaAs based devices, the closer the excitation is to the anode, the better yield can be expected [12, 7, 3]. The shape of the excitation spot is also crucial, and can prevent photoexcited particles from screening if extended in a certain direction [7].

[1] Therefore, at this point the Coulomb and the Radiated field is computed once more, but due to the short distance between the particle and it nearest point (smaller than a mesh cell), the delay does not need to be taken into account in the algorithm. Besides, we know that old radiated fields cannot directly reach its generator since they have a radial direction and propagate at a much higher speed than the particle itself.

Spatial shape

One can generate an elliptical Gaussian distribution of photons (x, y) around (x_0, y_0) by generating two numbers u_1 and u_2 randomly uniform between 0 and 1, and applying the following formula [11].

$$\begin{cases} x &= x_0 + \frac{a}{2}\sqrt{-2\log(u_1)}\cos(2\pi u_2) \\ y &= y_0 + \frac{b}{2}\sqrt{-2\log(u_1)}\sin(2\pi u_2) \end{cases} \tag{3.6}$$

Here a and b stand for the minor and major axes lengths of the elliptical Gaussian distribution. An example with a =1.2 µm and b =0.6 µm is displayed on Figure 3.3. When a photon is generated on a contact or outside the device, the corresponding electron-hole pair is not created.

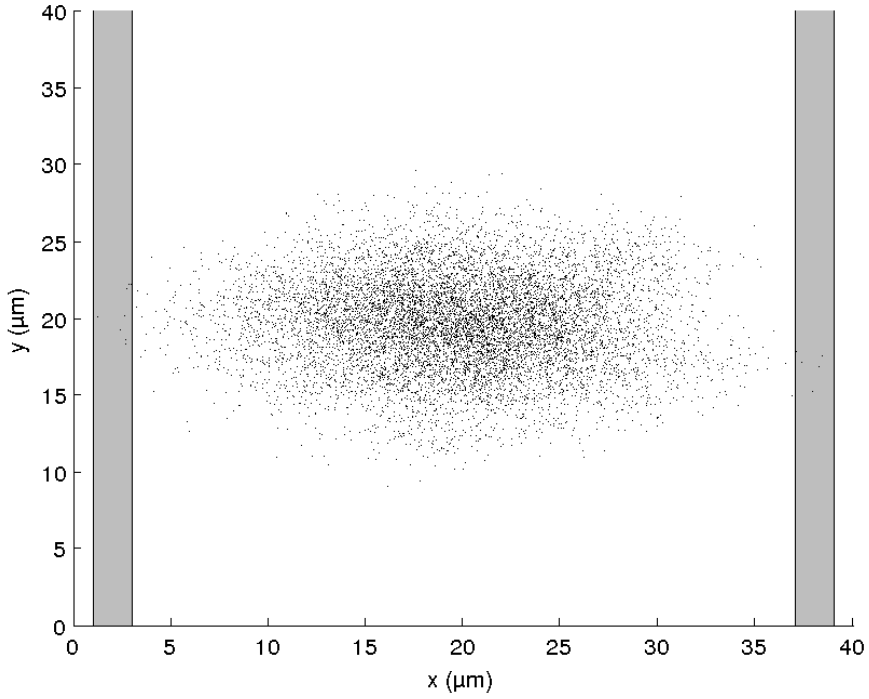

Figure 3.3: Generation of particles following a 2D-gaussian repartition

3.3.3 Laser temporal shape

The duration of the laser excitation can have a strong impact on the emitted THz radiation [3]. Our program can deal with this variable.

We assume our laser pulse generates a Gaussian shape of carriers over time. To provide a

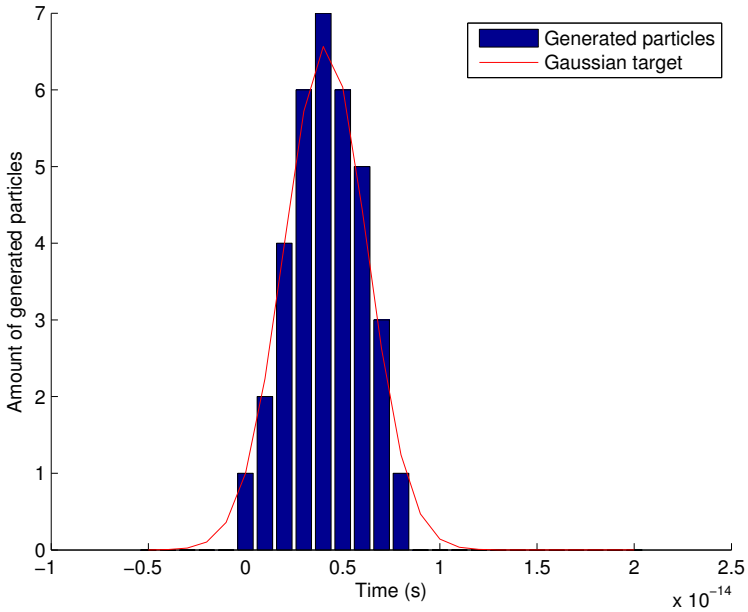

Figure 3.4: Generation of 35 particles following a Gaussian distribution, starting at t=0 s. δt = 1×10^{-15} s, σ =2.1233 $\times 10^{-15}$

discrete Gaussian distribution of a chosen amount $N_{particles}$ of particles, we need to know the number of particle expected in each bin of width δt, i.e. its integral between $t - \frac{\delta t}{2}$ and $t + \frac{\delta t}{2}$. We express this in term of the error function.

$$\mathrm{erf}(x) = \frac{2}{\sqrt{\pi}} \int_0^x e^{-t^2} \, \mathrm{d}t \tag{3.7}$$

$$n(t) = \left[\mathrm{erf}\left(\frac{t + \frac{\delta t}{2} - \mu}{\sqrt{2}\sigma} \right) - \mathrm{erf}\left(\frac{t - \frac{\delta t}{2} - \mu}{\sqrt{2}\sigma} \right) \right] N_{particles} \tag{3.8}$$

Where $\sqrt{2}\sigma$ widens the Gaussian distribution and μ shifts it so that the first set of particles begins at time 0. μ is computed as follows:

$$\mu = \begin{cases} \sigma \sqrt{2 \log\left(\frac{N_{particles} \delta t}{\sigma \sqrt{2\pi}} \right)} & \text{if } \frac{N_{particles} \delta t}{\sigma \sqrt{2\pi}} \geq 1 \\ 0 & \text{otherwise} \end{cases} \tag{3.9}$$

The full width at half maximum (FWHM) of the Gaussian laser pulse is specified by the user,

from which we compute σ:

$$\sigma = \frac{FWHM}{2\sqrt{2\log 2}} \tag{3.10}$$

From equation (3.8), $n(t)$ provides the integral of the Gaussian pulse envelope between $t - \frac{\delta t}{2}$ and $t + \frac{\delta t}{2}$. To make sure both that we generate an integer number of particle at each step and that the sum of the generated particles equals $N_{particles}$, the decimal parts of $n(t)$ are then gathered in the neighbouring timesteps to reconstruct the dismembered particles at the best possible time. An example of 35 particles generated with this technique is displayed Figure 3.4.

3.4 Material

The material plays a crucial role in the physical phenomenon. One should expect an improvement of THz emission for a material with a high electron mobility (lower effective mass)[8]. Many studies are carried out on GaAs or its alloys, or, more recently, on graphene [5]. Changing material in the program requires nonetheless to know all sort of physical constants related to electron dynamics, band structures and optical properties. Our studies are carried out on $Cd_xHg_{1-x}Te$, for it provides very small effective masses, and one can adjust the alloy fraction to get the physical parameters adjusted analogically. Since small bandgap implies smaller electron effective mass, and given that the band gap gets smaller as x decreases, the dynamics of the electrons can be adjusted at will. Materials with low band gap such as $Cd_xHg_{1-x}Te$ are expected to produce carrier pairs via impact-ionization scattering in a strong electric field. These carriers shall also contribute to the radiation.

3.5 Contacts

Usually, electrodes maintain the bias field by absorbing or supplying electrons/holes. When done in the program, the absorption/emission occurs instantaneously at each timestep, as if electrode conductivities were infinite. The timescales we work with are so small that one can assume that it is not enough to enable such an equilibrium [7, page 62]. Therefore, this process in the code has been disabled: electrodes are considered being too slow to give any feedback on our time window. Nonetheless, the background potential given by the resolution of Poisson

equation with our boundary conditions remains. Moreover, if an electron or a hole crashes into an electrode, it is absorbed and removed from the simulation to simulate the fact it carries on its way into the wire. As a side effect, its field becomes neglected instantaneously since we don't look at wire current radiation. Another side effect neglecting the dynamics at contact, is that we disregard hole injection at the anode, which is reported to emphasise the enhancement of the radiated field locally[12], but as shown later, the near-anode enhanced field can be exhibited even without hole injection.

Chapter 4

Results and discussions

4.1 Shape of the THz signal

Due to the bias field, electrons, once freed, will be accelerated to the anode, and hole to the cathode. The individual radiated fields (Figure 3.1) add up and generate a collective radiating field with a toroidal shape (Figure 4.1). After a fraction of a picosecond, electrons are either scattered or reach their limit velocity. As a result, only a radiation of tenths of picoseconds is emitted (Figure 4.2), falling in the range of the terhertz spectrum.

Due to the toroidal shape of the electric field, one gets most of the contribution only looking at the x-component above the device, and one can expect very low signal from points along the bias axis. The amplitude of the radiated field along this axis is computed for several distances above the device (Figure 4.3). One can notice the $1/r$ decrease as predicted by Equation 3.2, and that the noise gets much stronger close to the device. The noise is due to a stronger contribution from the particles near the detector as compared to the others, the simulation runs for a number of superparticles much smaller than the real amount of particles, therefore largely overestimates the noise which should be smoothed by statistics on an actual sample. On the same figure, a change of sign is also visible, implying a significant deceleration of the carriers.

In the rest of the study, we use five measuring points at the different positions indicated on Figure 4.4.

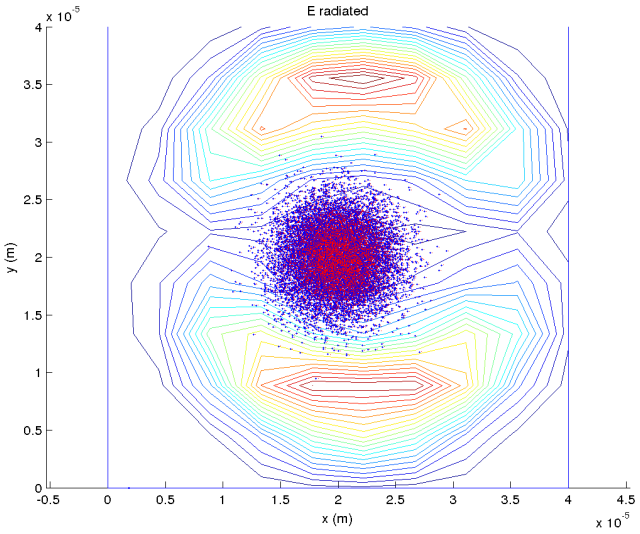

Figure 4.1: Electric field 1.8×10^{-13} s after the beginning of the laser pulse. Electrons appear in blue, holes in red. The apparent uneven partition between electron and holes is due to display issue only: for each hole, there is an electron slightly to its left.

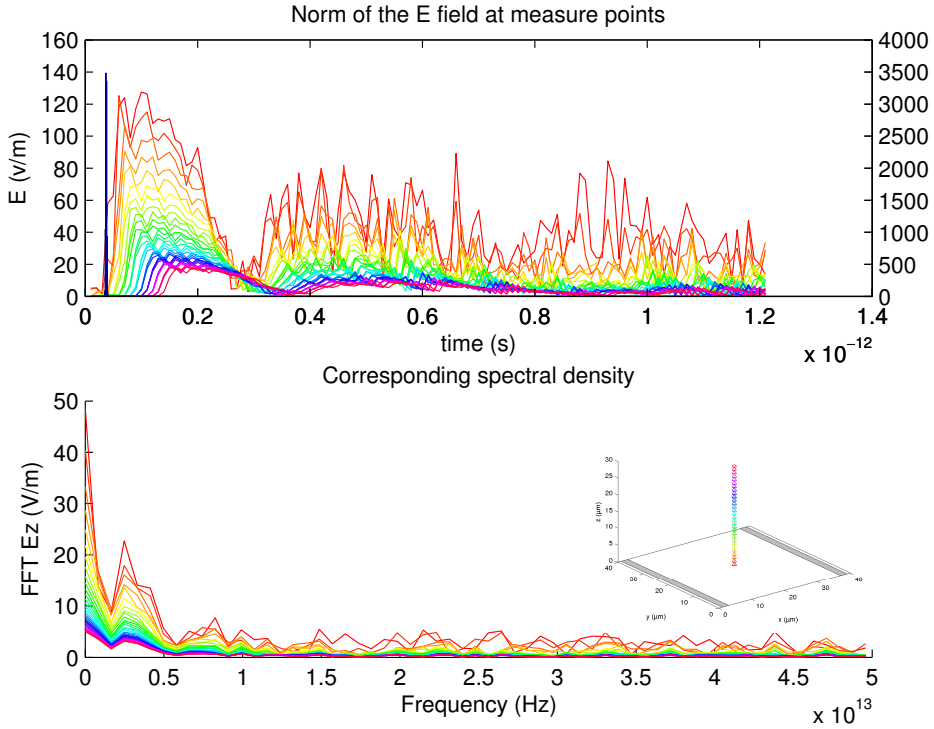

Figure 4.2: Norm of the radiated electric radiated field and corresponding spectrum at different points above the device, distant of 1 µm each, as a response of an optical excitation (Sharp blue peak in arbitrary vertical unit).

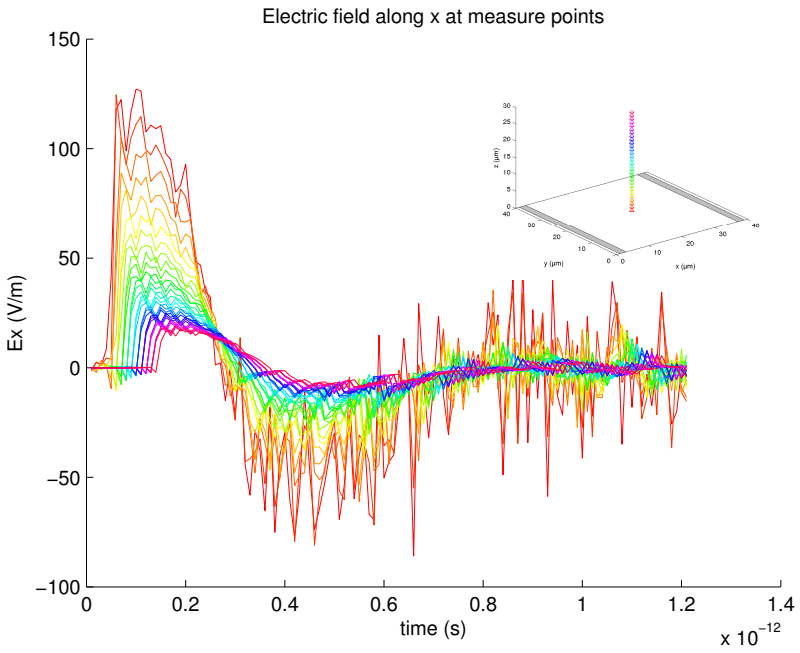

Figure 4.3: X component of the electric radiated field for 30 observation points increasingly distant of 1 µm above the device.

4.2 Role of the impurities

The negative part of the signal visible on Figure 4.3 is due to electrons slowing down when they scatter, in particular to L and X valleys [8, 7]. To evaluate this effect, a simulation was run on a material with poor impurity density, and with a sharp Gaussian **k** distribution to sharpen the positive peak (Figure 4.6a). On this figure, we can notice that after a short acceleration, carriers reach their maximum velocity and move freely on a relative large span before scattering, causing the deceleration. With a more physical optical **k** distribution, the initial peak is broadened and the deceleration occurs before all the carriers reach their limit velocity (Figure 4.8). With a very high amount of impurities, the peak gets shorter due to an early deceleration of the carriers, as shown on Figure 4.5.

Not surprisingly, the radiation signal is closely related to the drift acceleration of the electrons. Due to the lower mobilities of the holes, their drift quantities are approximately constant, significantly slower than the ones of electrons (holes drift velocity $2 \times 10^3\,\mathrm{m\,s^{-1}}$, holes drift acceleration $2 \times 10^{17}\,\mathrm{m\,s^{-2}}$), and therefore do not contribute as much.

In the rest of our simulations, the impurity density is chosen to be $10^{14}\,\mathrm{cm^{-3}}$. This value can

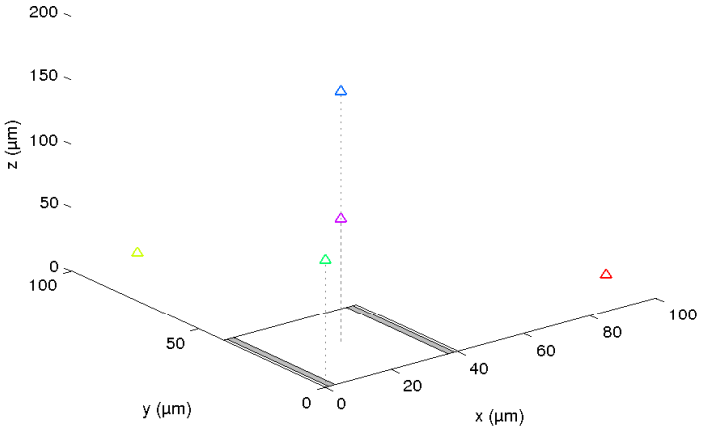

Point	x	y	z
1	100	20	0
2	20	100	0
3	0	0	100
4	20	20	200
5	20	20	100

Figure 4.4: Positions of the measuring points (in µm).

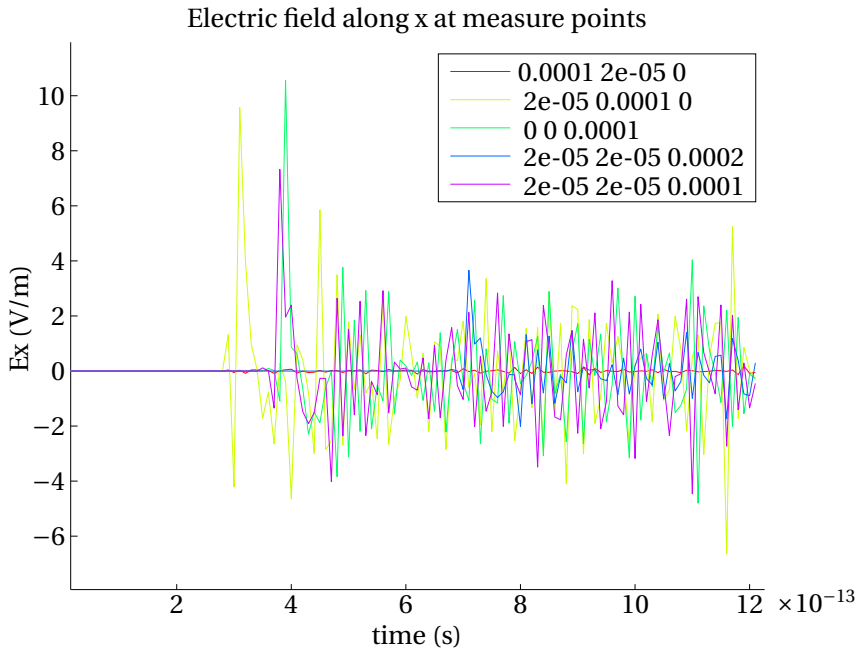

Figure 4.5: Optical excitation, on high impurity density material (10^{16} cm^{-3}) . The peak is short because the effective mass is larger and scattering occurs early.

be set in perspective with the density of photoexcited carriers: $10^{17}\,\mathrm{cm}^{-3}$.

4.3 Power of the laser

Increasing the laser input power is the most trivial way to get gain of power form the photoconductive switch. A high laser power leads to a higher carrier density, with higher energy. On Figure 4.10 is displayed the radiated power per carrier squared in function of the carrier density we got from our simulations. A straight line as we get should be expected because of the electrical power definition:

$$P \propto \int \|\mathbf{E}\|^2 \,\mathrm{d}t \tag{4.1}$$

$$\propto N^2 q^2 \langle \mathbf{a} \rangle^2 \tag{4.2}$$

Nonetheless, this situation is ideal. In practice one gets a saturation when the input power gets too high. This saturation is due to screening of the carriers. [7, p74] We failed to show this effect in our simulation on $\mathrm{Cd}_x\mathrm{Hg}_{1-x}\mathrm{Te}$. This might be a sign of a too primitive implementation of our screening mechanisms which does not manage to realistically reproduce the real behaviour of the electrons.

4.4 Bias field

Due to intervalley scattering only occuring at high voltage, the dynamics of the electrons at low ($5\,\mathrm{kV\,cm}^{-1}$) and at high ($40\,\mathrm{kV\,cm}^{-1}$) bias are known to differ dramatically in GaAs [7, p70]. In GaAs, THz emissions can be observed for bias starting at $500\,\mathrm{V\,cm}^{-1}$, but it is advised to aim higher than $4\,\mathrm{kV\,cm}^{-1}$ to get apreciable power[12, 7]. (It is worth mentioning that [12] notices that due to geometrical effects, a simple 4 V bias can be enough to produce a greater field than $4\,\mathrm{kV\,cm}^{-1}$ in the vicinity of the electrode.)

In this study, we focus on the high regime, setting our default bias to 160 V, thus targeting to an electric field of $40\,\mathrm{kV\,cm}^{-1}$. An increase of the bias of a few hundred volts is enough to see sign of saturation from the emitted field (Figure 4.10).

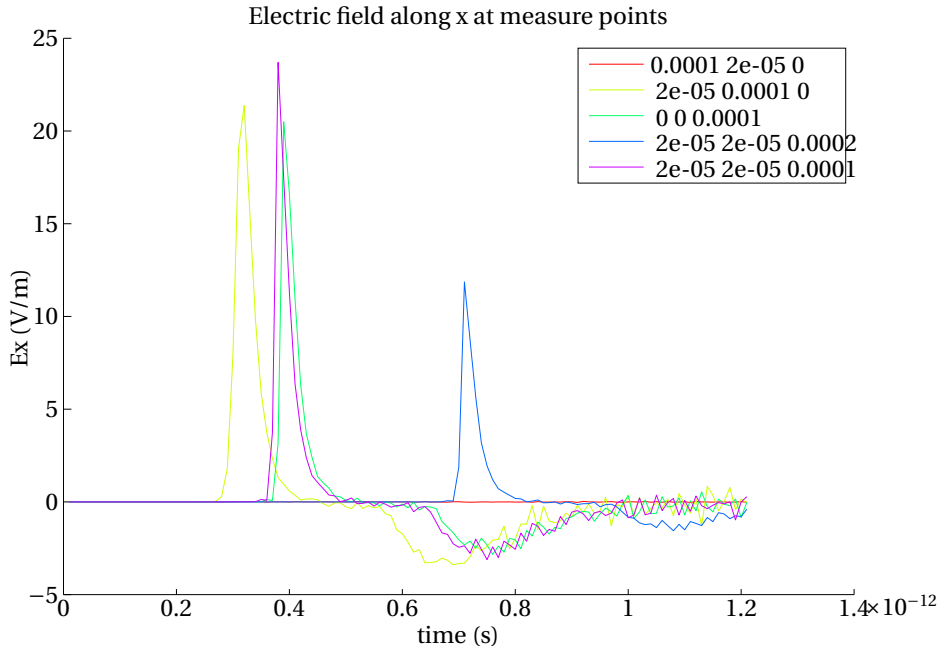

(a) Gaussian **k**-generation

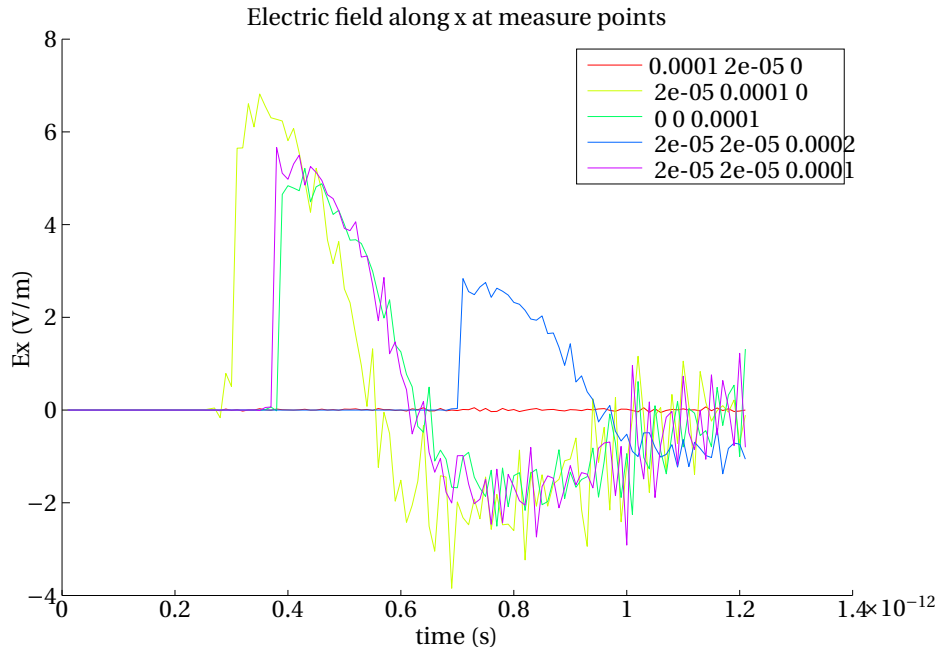

(b) Optical **k**-generation

Figure 4.6: Temporal shape of the parallel component of the radiated electric field for two different distribution of **k** at different observation points (coordinates in meter in the legend). Simulation for high purity material (impurity density 1×10^4 cm^{-3}), $Cd_xHg_{1-x}Te$ at 77 K. Simulation over 9000 particles. Photoexcited carriers density: 1×10^{17} cm^{-3}.

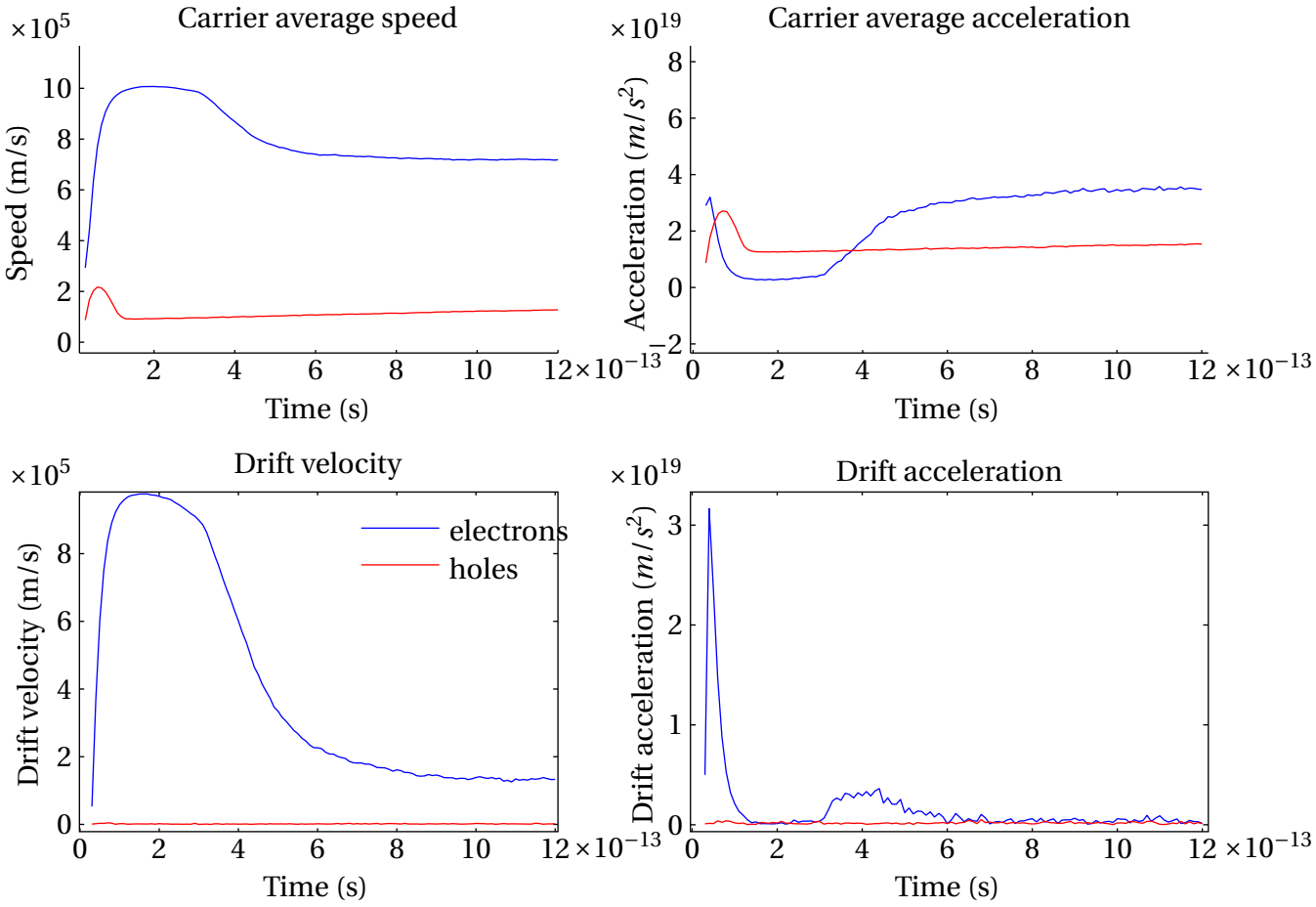

Figure 4.7: Mean values of speeds and accelerations of the carriers over time. Gaussian **k** distribution, low impurity (1×10^4 cm^{-3}).

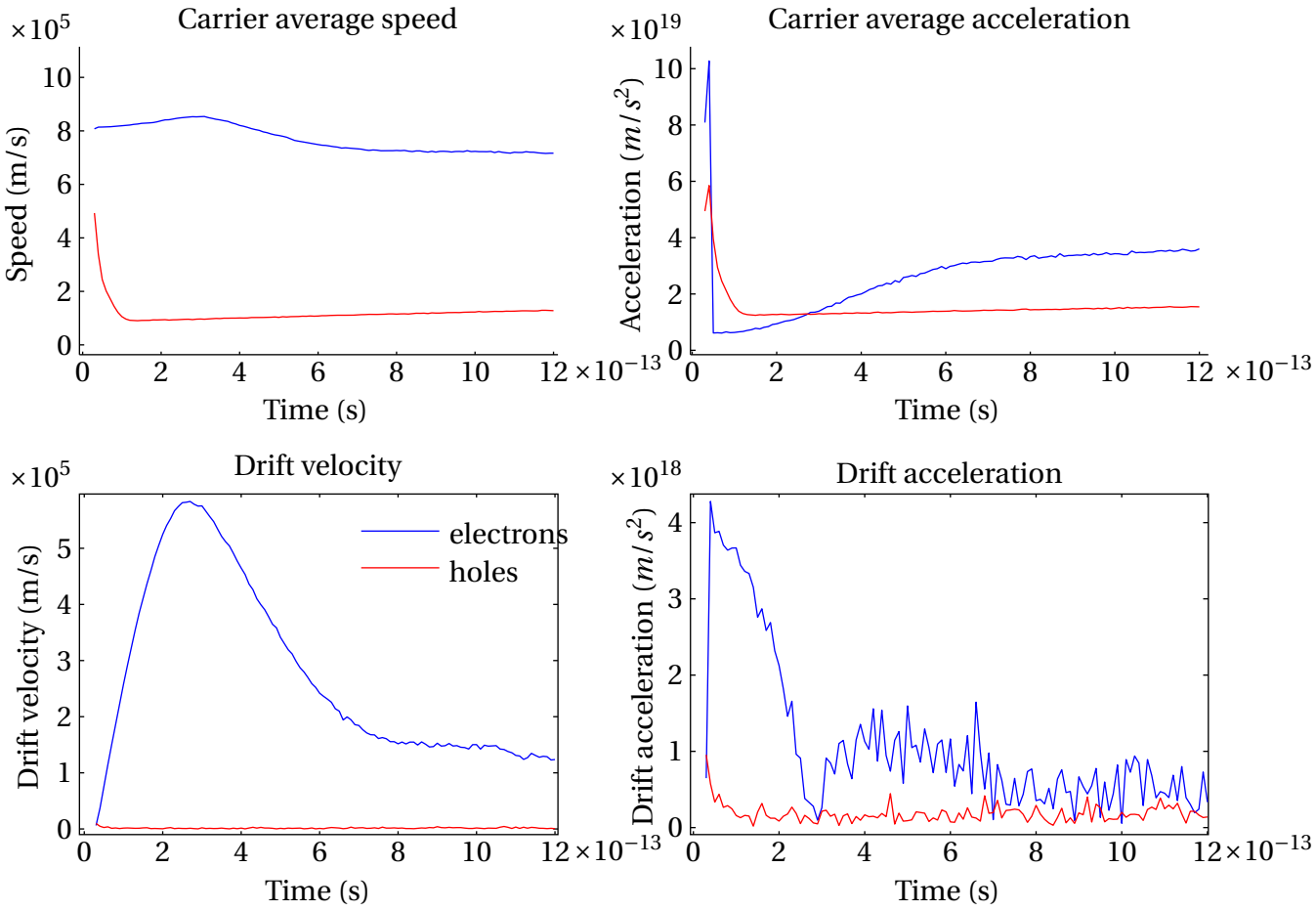

Figure 4.8: Mean values of speeds and accelerations of the carriers over time. Optical **k** distribution, impurity density: 1×10^{14} cm^{-3}.

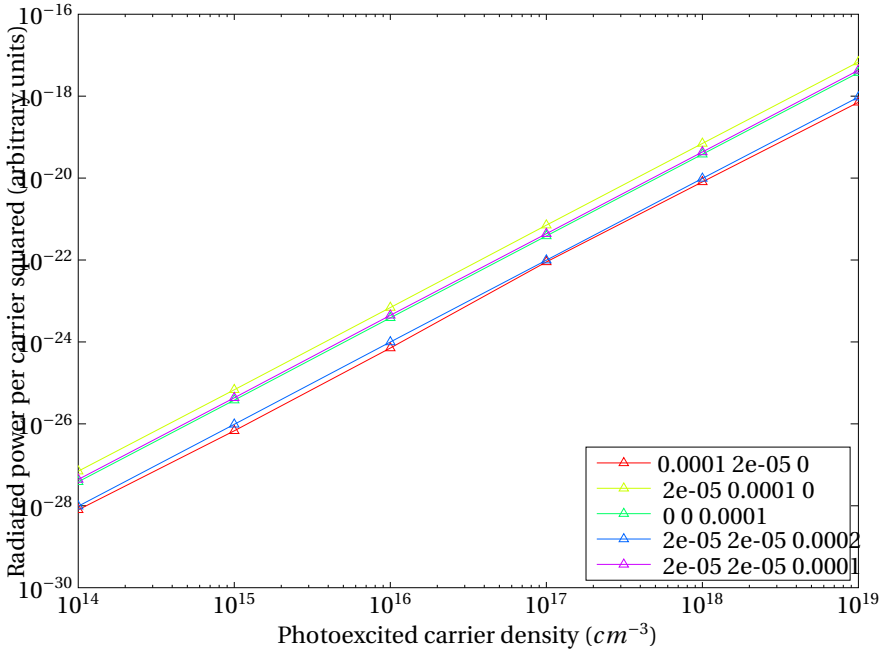

Figure 4.9: Radiation power per particle as function of the density of photoexcited carriers

4.5 Distance of the photoexcitation to the electrodes

The distance of the laser spot position with regard to the electrodes has been addressed repetitively on GaAs, and had been reported to greatly improve performances when the photoexcitation is close to the anode. This effect is mainly due to the difference in mobility of the two carriers, and can be enhanced with the appearance of trapped-enhanced fields at the proximity of the anode, or with carrier injection [3, 7, 12]. Our simulation can confirm this tendency in the case of $Cd_xHg_{1-x}Te$ as well (Figure 4.11). Figure 4.12 shows a relative increase of the power as one comes closer to the anode. The final decline close to the anode is due to the laser spot focusing in large part outside the device, therefore generating less carriers. Carrier injections and screening effects seems to play a secondary role in the mechanism, since our simulations with and without screening showed similar results. The radiation would be mainly due to a steeper potential near the electrodes, resulting in a stronger electric field. Electrons having a much higher mobility than the holes, the relative effect is visible near the anode.

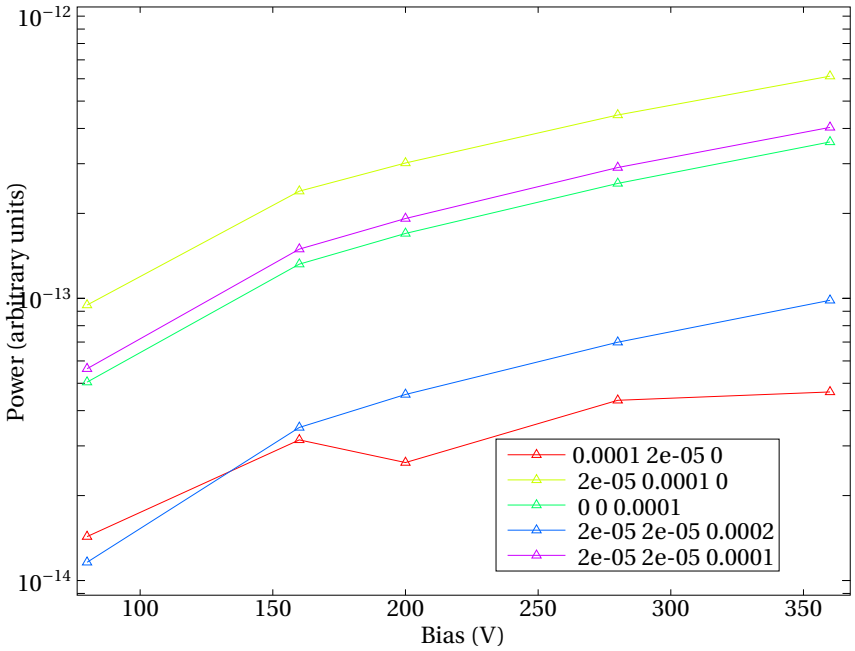

Figure 4.10: Radiation power per particle as function of the bias voltage

4.6 Duration of the excitation

The duration of the optical excitation can have an impact on the emitted radiation, because longer pulse introduce sharper energy, while favouring at the same time screening of the charges[3]. A too wide energy spectrum of the source can be counter-productive since it can either not be energetic enough to form exciton or be so powerful than it can cause electrons to jump into L valleys and increase effective mass. On the contrary, a too long energetically sharp pulse can cause extra screening.

Figure 4.13 attempts to show the tendency; a small decrease for pulses longer than 40 fs can be noticed for points above the device, but not significant enough to lead to conclusions. Especially not with the receivers in the plane of the device which show comparable increase. The effect is a priori independent of the number of carriers, even though a longer exposure to the optical excitation should moreover create more hole-electron pairs.

4.7 Shape of the spot

Finally comes the influence of the shape of the laser spot. This parameter is directly related to screening effects, and one should expect an improvement of terahertz emission as the area of

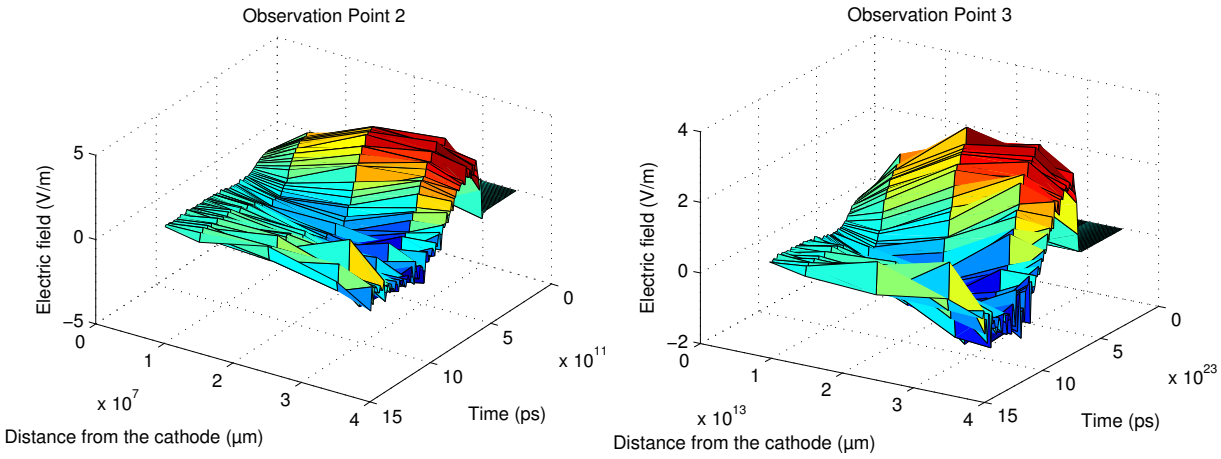

Figure 4.11: Strength of x component of the radiated field at observation points 2 and 3 (Figure 4.4) with respect to the distance of the excitation spot from the cathode.

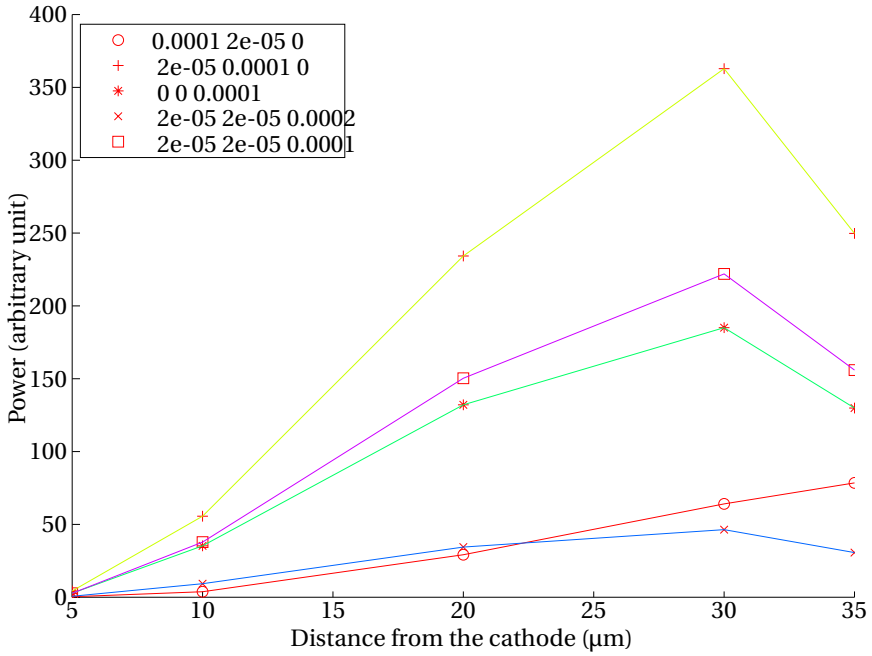

Figure 4.12: Power of the radiated field at observation points with respect to the distance of the excitation spot from the cathode.

the spot increases.

Both Coulomb and radiation screenings depend on the spot diameter, but Coulomb screening dominates radiation screening for small spots while radiation screening dominates larger spots.[7, p90], due to the respective power of the $1/R$ dependence.

One can also take advantage of the anisotropy of the experiment. Since the bias is along x, so is the motion of the carriers. Having an elliptic spot along this axis would reduce screening

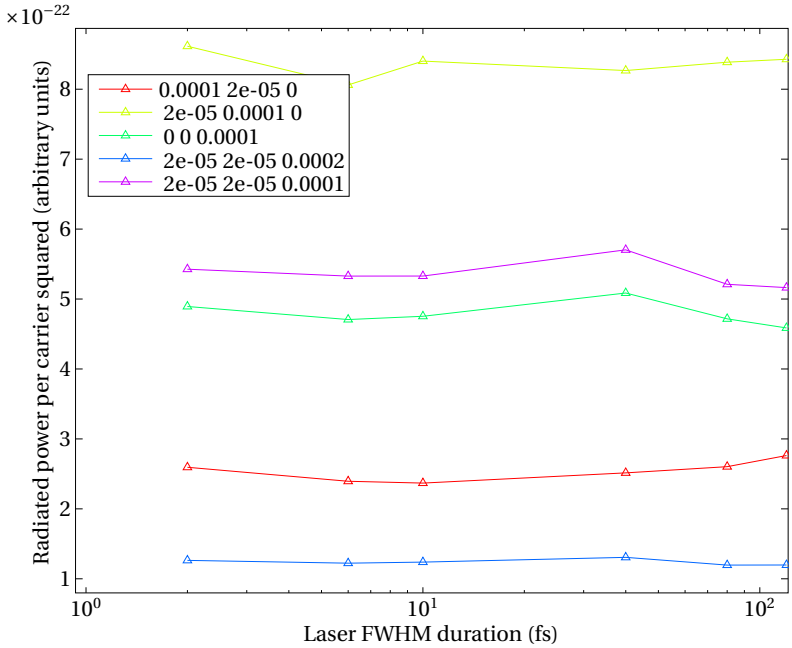

Figure 4.13: Dependence of the excitation duration on the radiated power per carrier.

[7], but as shown on Figure 4.14, our simulations would favour a circular shape.

Close to the anode, the predictions can nonetheless differ because of the local effect of the contact. In this case, it generally better to set the major axis of the ellipse along the anode.

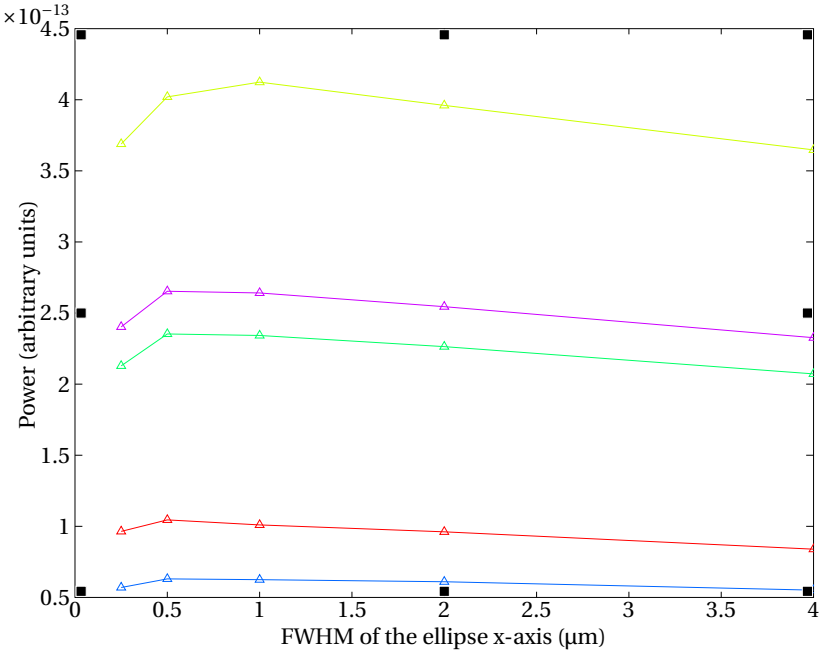

Figure 4.14: Radiative power with respect to the elliptical shape of the laser spot. The area of the spot is kept constant by seting the y-axis equal to the inverse of the x-axis.

Chapter 5

Summary and Recommendations for Further Work

5.1 Discussion

Even if we have been able to show several of the predicted effects, our simulator is not perfect and one should be aware of its flaws. The code should handle screening better. The current implementation seems stable, but no net effect have been noticed apart from those presented in the thesis. Likewise all the presented results could be improved with a higher mesh density, a larger number of superparticles, smaller time-step and longer simulation time. Results should always be cross-checked with actual physical experiments.

The generation of terhertz electromagnetic waves and their applications is a contemporary field of research which has led to many publications. Many known effects are not taken into account in our program, and would therefore fail to produce them without an update.

5.2 Recommendations for Further Work

Our simulator is so far only working in two dimensions, even if everything is transposable in three dimensions and that several methods in the code are ready to go three-dimensional. Existing commercial softwares, such as COMSOLimplement a 3D particles and a wave propagation model. It could be interesting to compare the results provided by the two programs, especially

with regard to the screening effects. Even though the kinetic model of COMSOL is not detailed enough to give extensive results at the present stage, one can hope for improvements in the future.

5.3 Summary and Conclusions

Through our simulator, we have exhibited the most typical phenomena of a photoconductive terahertz emitter device. Yet, the physics underlying remains extremely rich and would worth being studied longer. We used a semi-classical model for electron transport and took into account the delay of propagation of the electric field. We illustrated several phenomena and possibilities to increase the emission power. We showed that scattering and screening mechanisms were often responsible for power limitation and that a good understanding of them could lead to improvements. Thus, it is recommended to use a material with low impurities and which would provide a low effective mass, and apply a bias voltage of at least a few $10\,\mathrm{kV\,cm^{-1}}$. The laser should point at the anode and process to a powerful excitation as broad as possible spatially, during 40 fs. The receiver should be as close as possible from the device, in a radial position with respect to the bias axis.

Appendix A

Lorentz and Coulomb gauges

This appendix illustrates the main difference between Lorentz and Coulomb gauges.

A.1 Maxwell equations and potential definitions

The Ampère's circuital law is:

$$\nabla_{\times}\mathbf{H} = \mathbf{j} + \frac{\partial \mathbf{D}}{\partial t} \tag{A.1}$$

We assume having *scalar* quantities ε and μ such that:

$$\mathbf{D} = \varepsilon\mathbf{E} \tag{A.2}$$

$$\mathbf{B} = \mu\mathbf{H} \tag{A.3}$$

Potential fields ϕ and $\mathbf{A}$ are defined such that:

$$\mathbf{E} = -\nabla\phi - \frac{\partial \mathbf{A}}{\partial t} \tag{A.4}$$

$$\mathbf{B} = \nabla_{\times}\mathbf{A} \tag{A.5}$$

We can then write equation (A.1) in terms of potentials:

$$\nabla_{\times}\left(\frac{1}{\mu}\nabla_{\times}\mathbf{A}\right) = \mathbf{j} + \frac{\partial}{\partial t}\left(\varepsilon\left(-\nabla\phi - \frac{\partial \mathbf{A}}{\partial t}\right)\right) \tag{A.6}$$

Which, using vectorial identities expands as:

$$\nabla^2\mathbf{A} - \mu\varepsilon\frac{\partial^2\mathbf{A}}{\partial t^2} - \left[\nabla\left(\nabla.A\right) + \mu\varepsilon\frac{\partial\nabla\phi}{\partial t}\right] = -\mu\mathbf{j} - \frac{\nabla\mu}{\mu}\times\left(\nabla_\times\mathbf{A}\right) + \mu\frac{\partial\varepsilon}{\partial t}\left(\nabla\phi + \frac{\partial\mathbf{A}}{\partial t}\right) \tag{A.7}$$

The right hand side can be simplified according to the material's properties, but a coupling between $\mathbf{A}$ and ϕ will remain, at least in the left hand side. Fortunately, one can use the gauge freedom on $\nabla.\mathbf{A}$ to simplify the term into brackets.
In the following, we will consider $\nabla\mu$ and $\frac{\partial\varepsilon}{\partial t}$ equal to zero, leading to:

$$\nabla^2\mathbf{A} - \mu\varepsilon\frac{\partial^2\mathbf{A}}{\partial t^2} - \left[\nabla\left(\nabla.A\right) + \mu\varepsilon\frac{\partial\nabla\phi}{\partial t}\right] = -\mu\mathbf{j} \tag{A.8}$$

A.2 Gauges

Among many other possible gauges giving a constrain to $\nabla.\mathbf{A}$, we present here the consequences of Lorentz and Coulomb gauges.

A.2.1 Coulomb gauge

In Coulomb Gauge, $\nabla.\mathbf{A} = 0$, therefore the coupling of $\mathbf{A}$ and ϕ in equation (A.8) remains. This gauge is usually used to derive Poisson equation:

$$\nabla.D = \rho \tag{A.9a}$$

$$\nabla.\left(\varepsilon\mathbf{E}\right) = \rho \tag{A.9b}$$

$$\nabla.\left(\varepsilon\left(\nabla\phi + \frac{\partial\mathbf{A}}{\partial t}\right)\right) = -\rho \tag{A.9c}$$

$$\nabla\varepsilon\left(\nabla\phi + \frac{\partial\mathbf{A}}{\partial t}\right) + \varepsilon\left(\nabla^2\phi + \frac{\partial\nabla.\mathbf{A}}{\partial t}\right) = -\rho \tag{A.9d}$$

$$\nabla^2\phi + \frac{\partial\nabla.\mathbf{A}}{\partial t} = -\frac{\rho}{\varepsilon} \tag{A.9e}$$

where we assumed $\nabla\varepsilon = 0$. It is clear that the later equation simplifies into the Poisson equation in the Coulomb gauge:

$$\nabla^2\phi = -\frac{\rho}{\varepsilon} \tag{A.10}$$

The solution of Poisson equation is a instantaneous (non-retarded) potential ϕ. Whereas $\mathbf{A}$ is given by solving:

$$\mu\varepsilon\frac{\partial^2\mathbf{A}}{\partial t^2} - \nabla^2\mathbf{A} = -\left[\mu\varepsilon\frac{\partial\nabla\phi}{\partial t}\right] + \mu\mathbf{j} \tag{A.11}$$

This is a non-homogeneous d'Alembert equation, which means that $\mathbf{A}$ is a retarded field which depends on the instantaneous ϕ field. Because of the relatively complicated expression of $\mathbf{A}$, deriving $\mathbf{E}$ in this gauge can be cumbersome, this is why Coulomb gauge is mostly used in a static context.

A.2.2 Lorentz gauge

In Lorentz gauge, $\nabla.A = -\mu\varepsilon\frac{\partial\phi}{\partial t}$, therefore the term into bracket of equation (A.8) vanishes, along with the coupling. We are left with

$$\mu\varepsilon\frac{\partial^2\mathbf{A}}{\partial t^2} - \nabla^2\mathbf{A} = \mu\mathbf{j} \tag{A.12}$$

If we now try to derive Poisson equation in this gauge, assuming $\frac{\partial\mu\varepsilon}{\partial t} = 0$, we will get from equations (A.9)

$$\mu\varepsilon\frac{\partial^2\phi}{\partial t^2} - \nabla^2\phi = \frac{\rho}{\varepsilon} \tag{A.13}$$

Equations (A.12) and (A.13) are two independent d'Alembert equations with source terms. These equations have the so-called *retarded potentials* as solution, which are relatively simple to express. In the case of punctual charges, they can be simplified into the *Liénard-Wiechert potentials*.

A.3 Conclusion

We have shown that in a transient context, the Poisson equation must be obtained in the Coulomb gauge, which breaks symmetry between potentials ϕ and $\mathbf{A}$: the later being retarded and depending on the instantaneous former. In a non-static context, deriving $\mathbf{E}$ and $\mathbf{B}$ from them can become cumbersome, and the physical nature of the potentials themselves can be hard to get. On the other hand, the Lorentz gauge conserves symmetry and leads to two well-known independent retarded potentials ϕ and $\mathbf{A}$, which provides a much natural picture in a context of

radiation studies.

Despite the mentioned differences, we would like to highlight the fact that whatever the chosen gauge is, **E** and **B** will remain the same, and are always retarded.

Bibliography

[1] Ashcroft, N. W. and Mermin, N. D. (1976). *Solid State Physics*. Saunders.

[2] Berry, C. W. and Jarrahi, M. (2012). Terahertz generation using plasmonic photoconductive gratings. *New Journal of Physics 14 (2012) 105029 (12pp) doi:10.1088/1367-2630/14/10/105029*.

[3] Castro-Camus, E., Lloyd-Hughes, J., , and Johnston, M. (2005). Three-dimensional carrier-dynamics simulation of terahertz emission from photoconductive switches. *Physical Review B 71, 195301*.

[4] Ho1, L., Pepper1, M., and Taday1, P. (2008). Terahertz spectroscopy: Signatures and fingerprints. *Nature Photonics 2, 541 - 543 (2008) doi:10.1038/nphoton.2008.174* .

[5] Hunter, N., Mayorov, A. S., Wood, C. D., Russell, C., Li, L., Linfield, E. H., Davies, A. G., , and Cunningham, J. E. (February 24, 2015). On-chip picosecond pulse detection and generation using graphene photoconductive switches. *Nano Lett., 2015, 15 (3), pp 1591–1596 DOI: 10.1021/nl504116w* .

[6] Jackson, J. D. (1999). *Classical Electrodynamics*. Wiley, New York, 3rd edition.

[7] Kim, D. S. (August 2006). *Monte Carlo Modeling of Carrier Dynamics in Photoconductive Terahertz Sources*. PhD dissertation, Georgia Institute of Technology.

[8] Lloyd-Hughes, J., Castro-Camus, E., and Johnston, M. (2005). Simulation and optimisation of terahertz emission from InGaAs and InP photoconductive switches. *Solid State Communications 136 595–600*.

[9] Murakami, H., Fujiwara, S., Kawayama, I., and Tonouchi, M. (June 2016). Study of photoexcited-carrier dynamics in gaas photoconductive switches using dynamic terahertz emission microscopy. *Photon. Res. Vol. 4, No. 3 A9-A15*.

[10] Particles in cell consulting LLC (2010-2016). *Plasma Simulation*. URL: www.particleincell.com/blog.

[11] Press, W. H., Teukolsky, S. A., Vetterling, W. T., and Flannery, B. P. (1986-1992). *Numerical Recipes in Fortran 77: The art of scientific computing (ISBN 0-521-43064-X), Chap.7, p.279*. Cambridge University Press.

[12] Ralph, S. E. and Grischkowsky, D. (Oct 14 1991). Trap-enhanced electric fields in semi-insulators: the role of electrical and optical carrier injection. *Appl.Phys.Lett 59 (16)*.

[13] Sirtori, C. (May 9 2002). Applied physics: Bridge for the terahertz gap. *Nature 417, 132-133 doi:10.1038/417132b*.

[14] Stacey, G. J. (April 30 2008). New ground based facilities for THz astronomy. *9th International Symposium on Space Terahertz Technology, Groningen*.